ADVANCED ELECTRONIC MATERIALS
Open Access
www.advelectronicmat.de

Physical Reservoir Computing Utilizing Ion-Gating Transistors Operating in Electric Double Layer and Redox Mechanisms

Takashi Tsuchiya, Daiki Nishioka, Wataru Namiki, and Kazuya Terabe*

The enormous energy consumption of modern machine learning technologies, such as deep learning and generative artificial intelligence, is one of the most critical concerns of the time. To solve this problem, physical reservoir computing, which uses the non-linear dynamics exhibited by mechanical systems such as materials and devices as a computational resource for highly efficient information processing, has attracted much attention in recent years. In particular, ion-gated transistors, a group of devices that control electrical conductivity using electrochemical mechanisms such as electric double layers and redox, show very high computational performance with complex and diverse output properties in contrast to their simple structures, due to the complexity of the physical and chemical processes involved. This research provides an overview of physical reservoir computing using ion-gating transistors, focusing on the materials used, various computational tasks, and operating mechanisms.

1. Background Story of Physical Reservoir Computing and Ion-Gating Transistors

Nowadays, the development of machine learning, represented by deep learning and generative AI, has transformed modern life depending on information.[1] The ability to learn and analyze vast amounts of information that would be unmanageable to humans and to generate various types of digital content such as natural text, images, music, and movies, which previously could only be produced by humans, is the result of advances in AI software running on computers.[2] However, while machine learning has rapidly grown into a versatile tool, it is also causing severe social problems. That is the vast power consumption associated with running high-load information processing on conventional computers with von Neumann architecture.[3] To solve this problem, more than conventional software improvements are needed, but the computer that performs the information processing, i.e., the hardware, needs to be improved. From this perspective, neuromorphic computing has attracted attention in recent years. For example, the physical implementation of hierarchical neural networks using semiconductor circuits based on CMOS or memristors allows mainly sum-of-products operations to be processed with low power consumption.[4–8] In this case, the operation is performed by expressing the connection weights, corresponding to the connection strengths between neurons in biological neural networks, using the electrical resistances in the physical elements. Although this method can, in principle, reproduce any hierarchical neural network and can be expected to consume considerably less power, a high information processing load is still unavoidable for recording and updating the large number of connection weights used in general deep learning. For this reason, reservoir computing has been recently considered a promising solution to these problems and to achieve further low-power consumption through neuromorphic computing.[9–12]

Reservoir computing (RC) is a machine learning framework derived from the recurrent neural network model with recurrent structures inside the network, unlike a multi-layer neural network with a hierarchical structure.[9] The two models are compared in **Figure 1**a. A reservoir network consists of a reservoir, of which function corresponds to the hidden layers (interlayers) of multi-layer neural networks and transforms the input data, and a readout, where the reservoir remains unchanged and fixed during the learning process. The readout uses a learning mechanism such as a linear learner algorithm to train (update) the connection weights (W). Since the number of W is far smaller than deep learning, reservoir computing enables fast learning. Detailed background of RC was reported elsewhere.[9–12] In particular, physical reservoir computing (PRC) has attracted attention because information processing inside the reservoir can

---

T. Tsuchiya, D. Nishioka, W. Namiki, K. Terabe
Research Center for Materials Nanoarchitectonics (MANA)
National Institute for Materials Science (NIMS)
1-1 Namiki, Tsukuba, Ibaraki 305-0044, Japan
E-mail: TSUCHIYA.Takashi@nims.go.jp

D. Nishioka
International Center for Young Scientists (ICYS)
National Institute for Materials Science (NIMS)
Sengen 1-2-1, Tsukuba, Ibaraki 305-0047, Japan

The ORCID identification number(s) for the author(s) of this article can be found under https://doi.org/10.1002/aelm.202400625

DOI: 10.1002/aelm.202400625

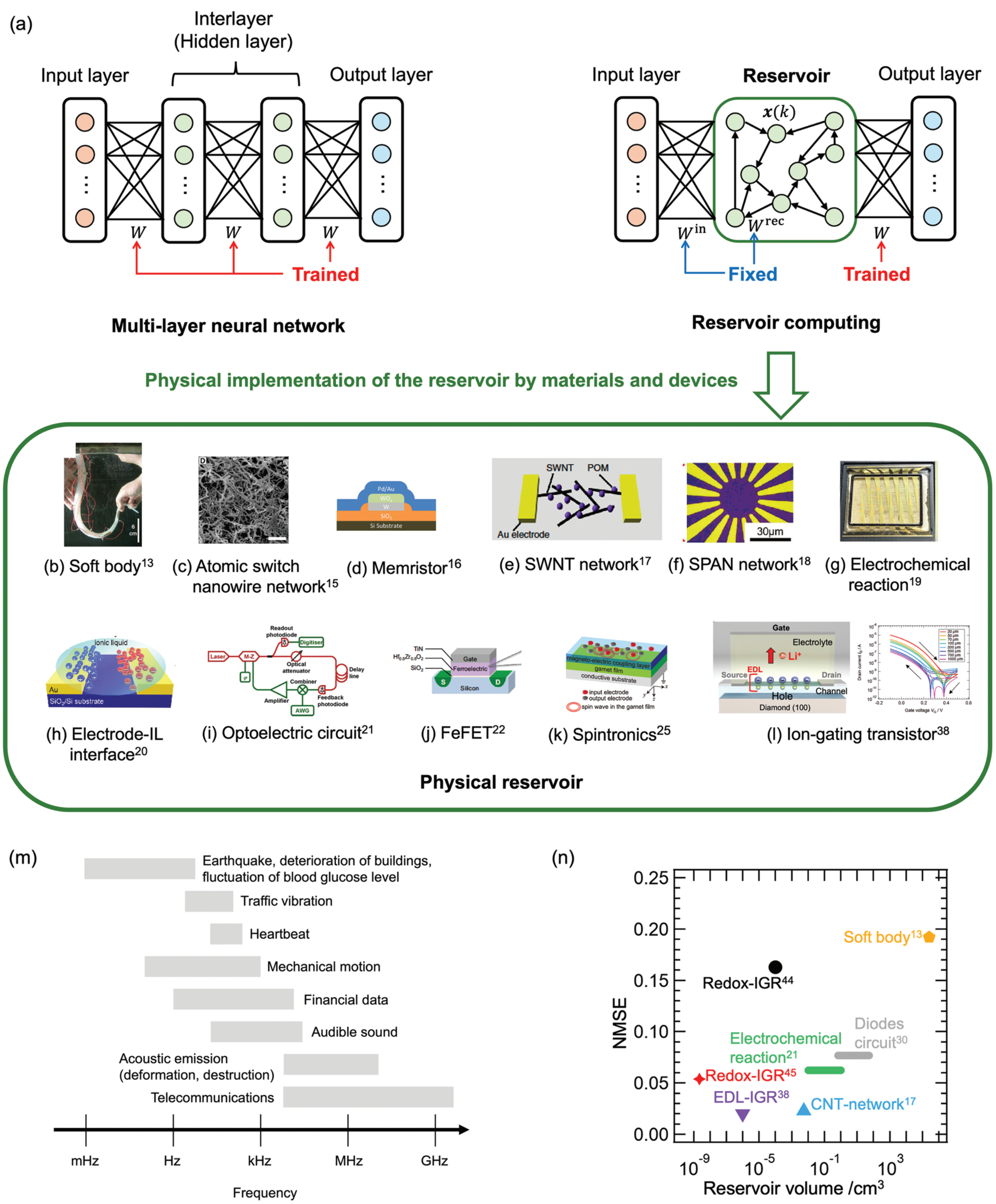

Figure 1. a) Comparison with multi-layer neural network and reservoir computing models. b–l) various physical reservoir computing materials and devices.[13,15–22,25,38] Reproduced with permission.[13] Copyright 2015, Springer Nature. Reproduced with permission.[15] Copyright 2021, Frontiers Media SA. Reproduced with permission.[16] Copyright 2017, Springer Nature. Reproduced with permission.[17] Copyright 2022, IOP Publishing. Reproduced with permission.[18] Copyright 2021, Wiley. Reproduced with permission.[19] Copyright 2022, Wiley. Reproduced with permission.[20] Copyright 2022, Springer Nature. Reproduced with permission.[21] Copyright 2012, Springer Nature. Reproduced with permission.[22] Copyright 2022, Springer Nature. Reproduced with permission.[25] Copyright 2018, IEEE. Reproduced with permission.[38] Copyright 2022, the American Association for the Advancement of Science. m) Comparison with frequency range of various events for PRC applications. n) Computing performance (normalized mean square error for NARMA2 task)-reservoir volume relationship of reported PRC devices with relatively small reservoir volume. Reproduced with permission.[45] Copyright 2023, Springer Nature.

instead be physically implemented using the nonlinear response of materials and devices, known as "physical reservoirs".[11]

For example, in a PRC using a soft silicone arm immersed underwater as a physical reservoir, typical time series data predictions such as nonlinear autoregressive moving-average (NARMA) tasks were performed using the complex arm motion in a water tank, which was detected by bend sensors embedded within the arm, as shown in Figure 1b.[13] Figure 1c shows a physical network of an atomic switch, a resistive switching device operating in the reversible generation and annihilation of metallic nanofilaments, applied to PRC.[14,15] The electrical response of self-assembled nanowire networks was utilized for waveform generation and spoken digit classification. A cross-bar array of WO_x thin film-based resistive switching devices, memristors, are applied to PRC, as shown in Figure 1d.[16] Nonlinear electrical behaviors of networks consisting of single-walled carbon nanotube (SWNT) or sulfonated polyaniline (SPAN) were utilized to perform PRC, as shown in Figure 1e,f.[17,18] The ionic current response of an electrochemical cell with polyoxometalate (POM) solution or ionic liquid (IL) was applied to time series data processing, as shown in Figure 1g,h.[19,20] In PRC using an opto-electric circuit with a Mach-Zehnder modulator and delay line, benchmark tests such as NARMA and spoken digit recognition were performed, as shown in Figure 1i.[21] Electrical response accompanied by polarization reversal of ferroelectric field effect transistors (FeFETs) with a HfO_2-based ferroelectric thin film, as shown in Figure 1j, was applied to second-order nonlinear dynamic equation tasks.[22] Related to spintronics technologies, the fast nonlinear response in the MHz to GHz band obtained by spin torque oscillators and spin-wave interference was used, as shown in Figure 1k.[23–29] There are many other examples besides these.[30–37]

Recently, one class has shown exciting developments. That is, ion-gating transistors-based PRCs.[38–48] Ion-gating transistors are understood based on replacing the dielectric layer of a typical field-effect transistor with an ion-conducting material. They can tune the electrical conductance of semiconductor channels by using a variety of ionic behaviors, as shown in Figure 1l.[38] For performing PRC, information is input to a physical reservoir, and its transient response is used as a computational resource, so the time constant of the input information and the time constant of the response of the physical reservoir are desired to be close for minimizing the additional processing costs.[49] In practical use, the physical reservoirs are required to respond to a wide range of time constants because the physical reservoirs input and process a variety of information (e.g., mechanical motion, audible sound, blood glucose level, heartbeat, financial data, earthquake) in the environment measured in real-time by sensors and other means, as shown in Figure 1m. However, physical phenomena generally have inherent time constants, and it is difficult to modulate them significantly, except for analog electrical elements unsuitable for integration.

In contrast, time constants electrical response in ion-gating transistors can be widely modulated from microseconds to over 1000 s due to the varied transport properties of mobile ions and electrons in ion-conducting materials. In contrast, ion-gating transistors have a simple structure consisting of thin layers of electrolyte thin films and semiconductors,[42,50–58] making the ion-gating transistors attractive in the aspect of computing performance-reservoir volume relationship as shown in Figure 1n.[42,50–58] The ion-gating transistor is thus a promising PRC platform compatible with wide response speed, high integrity, and high computing performance. This article reviews recent advances in state-of-art PRCs based on ion-gating transistors from aspects of the operation mechanism of ion-gating transistors, including the electric double layer (EDL) effect and redox reactions, and the PRC performance and characteristics as physical reservoirs.

2. Operation Mechanisms of EDL and Redox Transistors

Ion-gating transistors are field-effect transistors in which the electrical conductance of the semiconductor channel is modulated by electronic carrier density tuning through the EDL effect or redox in the vicinity of the electrolyte/semiconductor channel interface.[50–58] **Figure 2a,b** shows schematic illustrations of EDL and redox transistors comprising a Li^+ conducting electrolyte. Both transistors seemingly have a common FET structure comprising electrolyte, semiconductor channel, and electrodes, including source, drain, and gate. The one significant difference between them is the occurrence of ion transfer, resulting in ion insertion into the semiconductor channel: ion insertion occurs in redox transistors due to the ion (chemical) capacity of the semiconductor channel but does not happen in EDL transistor (EDLT) due to ion-blocking property of semiconductor channel. In the operation mechanism of EDLT shown in Figure 2a, the mobile ion in the electrolyte is driven toward the semiconductor channel or gate electrode under the V_G-applied conditions. EDL, with the electric charge of ion/vacancy in the electrolyte and electronic charge with the opposite polarity in the semiconductor channel surface, is formed in the vicinity of the electrolyte/semiconductor channel interface to modulate electronic carrier density of the surface of the semiconductor channel along the relationship $Q = C_{EDL}V$, where Q, $C_{EDL,}$ and V are accumulated charge density, EDL capacity, and voltage applied to the interface.[51] This corresponds to the Fermi level (E_F) shift on the surface of the semiconductor channel, as shown in the lower panel of Figure 2a. Since C_{EDL} is known to exceed several μF cm^{-2}, EDLT has excellent carrier density tunability. In particular, electronic carrier doping by EDLT does not introduce defects in the semiconductor channel, which is advantageous to maintain electron mobility even under high-density electronic carrier conditions.

On the other hand, in the operation mechanism of redox transistors shown in Figure 2b, mobile ions in the electrolyte, driven by the applied V_G, are inserted into the semiconductor channel. This causes a redox reaction, leading to variation in E_F accompanied by electronic carrier density, as shown in the lower panel of Figure 2b. Suppose we assume an oxide semiconductor MO_x as the semiconductor for example. It corresponds to the redox reaction of component ions in the semiconductor channel $M^{n+} + e^- \rightarrow M^{(n-1)+}$, resulting in electronic conductivity modulation in the semiconductor. Since typical semiconductor channel materials for redox transistors have a large chemical capacity reaching 10^{21} cm^{-3}, huge electronic conductivity tuning is also possible for redox transistors. One notable difference in the carrier doping behavior between redox transistors and EDLTs is electronic carrier

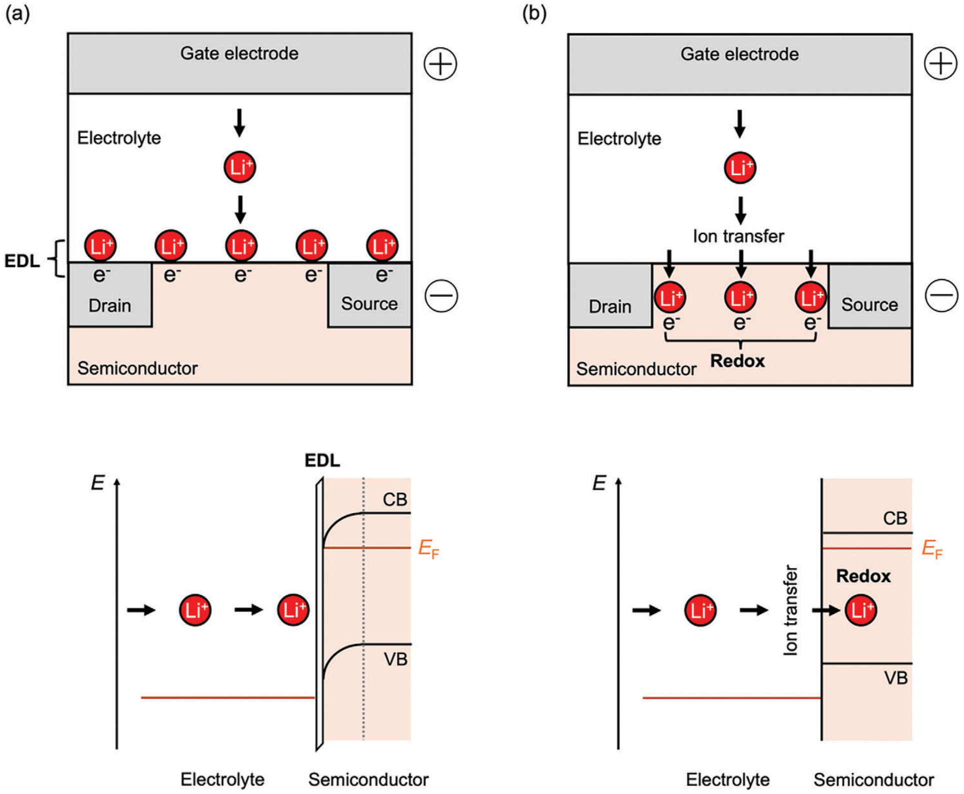

Figure 2. Operation mechanisms and the corresponding energy diagrams of a) EDLT and b) redox transistor.

distribution in the semiconductor channel. Whereas doped electronic carriers are accumulated on the surface of the semiconductor channel for EDLTs, those are basically distributed in the whole area of the semiconductor channel for redox transistors, as described in the lower panels of Figure 2. This can affect the electrical response of the transistors. Since relatively slow ion/electron transport in the whole channel is involved in the electrical response, redox transistors tend to show a slow electrical response compared to EDLTs. As a wide range of response time (time constant) is required for PRC toward practical use, the wide variety of time constants in electrical response is the attractiveness of ion-gating transistors. Furthermore, the electrical response is under the influence of electric carrier transport/transfer processes included in the transistors' layered structure, enhancing the electrical response's diversity and complexity in contrast to the apparently simple structure.

3. Physical Implementation of RC with Ion-Gating Transistors

A primary function of physical reservoirs in PRC is mapping input $u(k)$, which is time series data at discrete time step k, to high dimensional feature space through the nonlinear response of the physical reservoir.[12] **Figure 3a** shows a schematic illustration of the general PRC processing. In the N-dimensional feature space with reservoir states X_i ($i = 1, 2, 3 \ldots N$), pattern recognition of different labels, which are included in $u(k)$, by separating hyperplanes becomes possible. As an example, the relationship between $u(k)$, $X_i(k)$ and mapping function f_i for the case in which is dependent on $u(k)$ and $X_i(k-1)$, which is $X_i(k)$ for one step past $k-1$, is given as follows;

$$X_i(k) = f_i\left[u(k),\ X_i(k-1)\right] \tag{1}$$

This property of $\boldsymbol{f} = (f_1, f_2, .., f_n)$, nonlinear transformation capability of $u(k)$ to the high dimensional feature space is termed as "nonlinearity" of physical reservoirs. In simpler terms, nonlinearity is understood as a nonlinear relationship between input and output. The role of physical reservoirs in PRC is the physical implementation of $\boldsymbol{f}$ and a connected network structure between reservoir states by the nonlinear response of materials or devices. As a broad argument, if one could give an example similar to the function of physical reservoirs, it would be a frequency-selective filter, in which an original signal is transformed into another signal with different frequency components. However, in the case of PRC, the relationship among each state in the time domain can be learned, making the PRC significantly useful for versatile information processing.

For the PRC's better performance, high dimensionality, and short-term memory, as well as nonlinearity, are required for physical reservoirs. High dimensionality and short-term memory can be interpreted as versatility of output, and capacity to temporally store information input to the materials or devices, respectively. While the former makes pattern recognition by separating hyperplanes easier thanks to a sufficient degree of freedom in the higher dimensional feature space, the latter is for learning temporal dynamics of $u(k)$. In the cases with fully-simulated RC, $\boldsymbol{f}$ $\left(f_i = f_j, i \neq j\right)$ is explicitly described in mathematic

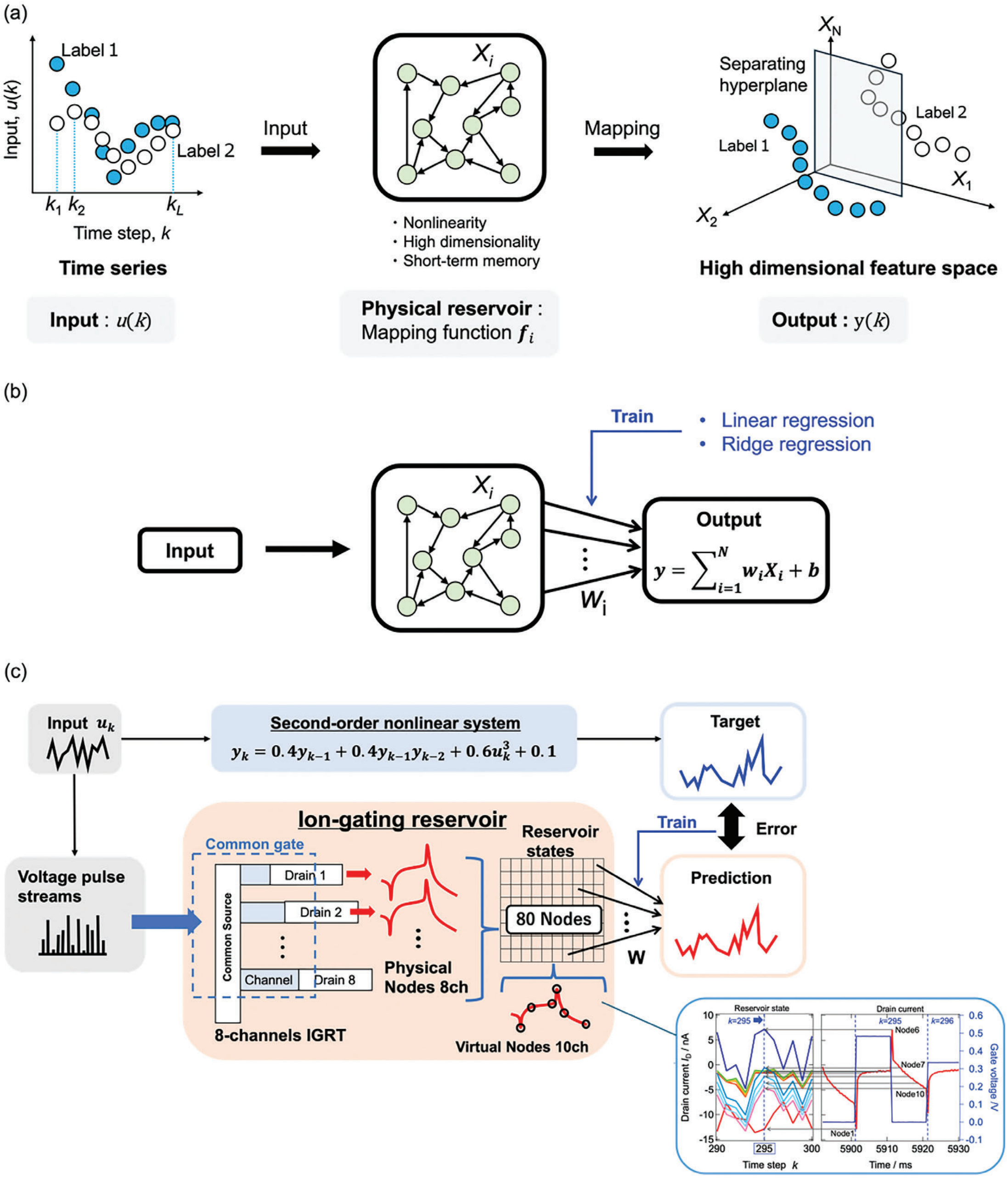

Figure 3. a) A schematic illustration of the general PRC processing. b) a schematic illustration of RC. c) A schematic of the second-order nonlinear dynamic equation task with an ion-gating reservoir.[38] Reproduced with permission.[38] Copyright 2022, the American Association for the Advancement of Science.

expression and simulated on the CPU-based computation. On the other hand, in the cases with PRC, *f* and a connected network structure between reservoir states are embedded in physical reservoirs as inherent materials characteristics and generally dependent on various operating conditions, making *f* complex $\left(f_i = f_j, i \neq j\right)$. Although it is not straightforward to clarify the exact expression of *f*, the characteristic is advantageous for obtaining diverse output and resulting in high performance.

Figure 3b shows a schematic illustration of RC. The reservoir output $y(k)$ at discrete time step k is obtained by the linear combination of reservoir state $X_i(k)$ and readout weight W_i as follows;

$$y(k) = \sum_{i=1}^{N} W_i X_i(k) + b \tag{2a}$$

$$= \boldsymbol{W}\boldsymbol{X}(k) + b \tag{2b}$$

where b is the bias; N is the reservoir size; $\boldsymbol{W} = (W_1, W_2, \ldots, W_N)$ is the readout weight vector; $\boldsymbol{X}(k) = [X_1(k), X_2(k), \ldots, X_N(k)]^{\mathrm{T}}$ is the reservoir state vector.[40] A typical task execution process with a PRC consists of training and test phases. In the training phase, W_i are trained by linear regression or ridge regression to minimize error between $y(k)$ and the model output $y_t(k)$, which is generated by equations corresponding to specific tasks. In the test phase, W_i are fixed, and PRC performance is evaluated based on error between $y(k)$, corresponding to the prediction waveform, to $y_t(k)$ for a different input $u(k)$ than in the training phase. Therefore, consistency in the non-linear mapping of the reservoir to the inputs is essential for the trained W_i to work effectively with unknown data. This is also referred to as the echo-state property and is achieved by adjusting the topology of the network structure and the spectral radius related to the recurrent weights in the case of simulated RC, whereas in the case of PRC, it is achieved by introducing deterministic non-linear dynamics and improving the signal-to-noise in the state observation. Normalized mean square error (NMSE) is used as an appropriate error suitable for comparison.

$$\mathrm{NMSE} = \frac{1}{M}\frac{\sum_{k=1}^{M}\left[y_t(k) - y(k)\right]^2}{\sigma^2\left[y_t(k)\right]} \tag{3}$$

where M is the data length; $\sigma^2(\cdot)$ is the variance. The NMSE is also often introduced as an error normalized by the sum of squares of the target data, as follows;

$$\mathrm{NMSE} = \frac{\sum_{k=1}^{M}\left[y_t(k) - y(k)\right]^2}{\sum_{k=1}^{M}\left[y_t(k)\right]^2} \tag{4}$$

Mean square error (MSE) and root mean square error (RMSE) are alternatively used. Since these are entirely different, comparing PRC performance by mixing these makes no meaning.

The PRC scheme discussed above is outlined below, taking the second-order nonlinear dynamic equation task with an EDLT (ion-gating reservoir transistor, IGRT) as an example.[38] A schematic of the task is shown in Figure 3c. The target (model output) $y_t(k)$ for the task is expressed by the following equation;

$$y_t(k) = 0.4y_t(k-1) + 0.4y_t(k-1)\,y_t(k-2) + 0.6u^3(k) + 0.1 \tag{5}$$

where k and $u(k) = [0,0.5]$ are discrete time steps and a random input that were applied to IGRT as gate voltage (V_G) pulse streams, respectively. The reservoir states $X_i(k)$ were obtained from the drain current (I_D) response, which is widely varied by the strong influence of V_G application hysteresis, as discussed in the former section. The reservoir output $y(k)$ is the linear combination of $X_i(k)$ and readout weights W_i trained in the manner discussed along equations 2a and 2b. The physical node is defined as the terminal in which $X_i(k)$ is experimentally measured and corresponds to the drain electrode in the present case.

One notable advantage of a transistor structure is that increasing physical nodes is easily achieved merely by increasing the drain electrodes, in contrast to other PRC devices, which have a limited degree of freedom for device structure or materials nature.[13,21] In the present example, the IGRT has an 8-channel (drain)-1-gate-1-source structure with 8 different channel lengths, as shown in Figure 3c. The 8 different drains give 8 physical nodes in the RC. By applying the V_G pulse stream, which is converted from $u(k)$, to the common gate, 8 different I_D responses are measured from the 8 drains. Since one V_G pulse corresponds to $u(k)$ at a discrete time step k, the real-time evolution of I_D during V_G pulse application and the following interval, I_D can provide multiple reservoir states from each time; virtual nodes. 10 virtual nodes are obtained from each of 8 different I_D responses, as shown in the right panel of Figure 3c. Accordingly, the IGRT provides 80 nodes in total. The target waveform is reproduced from a linear combination of the 80 nodes (reservoir states $X_i(k)$) with 80 readout weights W_i. Through the training and test phases discussed above, PRC is performed.

4. PRC Using Ion-Gating Transistors

4.1. PRC Using EDL-based Ion-Gating Transistors

The application of EDL transistor (EDLT) to PRC was first reported by Nishioka et al.[38] Their EDLT comprises of Li^+ conducting Li-Si-Zr-O (LSZO) amorphous thin film and hydrogen-terminated diamond single crystal (100) was applied to PRC, as shown in **Figure 4a**.[38] As the hydrogen-terminated diamond shows excellent p-type semiconduction due to the two-dimensional hole gas (2DHG) on the hydrogen-terminated surface, the electrical conductance is widely controllable in the four orders of magnitude by reversible EDL charging–discharging at the diamond/LSZO interface under the small V_G application.[59] Since the surface p-type conduction of the diamond channel strongly affects on Li^+ transport as the channel resistance works as an additional resistance to an electrical resistance for Li^+ transport resistance of LSZO thin film, the electrical response of the EDL charging–discharging, including Li^+ and hole transport, is sensitive to the current condition of EDL charge at the location, as termed as ion-electron coupled dynamics. Thanks to the mechanism, the EDL-based ion-gating reservoir (IGR) showed diverse drain current output with a variety of relaxation times and spike intensities, leading to enhanced high dimensionality (diversity of output), as shown in Figure 4b. The reservoir states obtained from the drain currents were useful for performing hand-written digit recognition with the MNIST dataset. As shown in Figure 4c, EDL-based IGR showed excellent performance in spite of a very small network size compared to a three-layer neural network.[38] Furthermore, a more difficult benchmark task termed the second-order nonlinear dynamic equation task, was performed. Schematic of the task performed by the EDL-IGR is shown in Figure 3c. Reservoir states were from the real-time electrical response of the EDLT. **Figure 5a** shows a comparison between the target waveform (generated by the second-order nonlinear dynamic equation) and prediction waveform (generated from the EDLT output) with a very small deviation (error). The EDL-IGR showed outstanding prediction accuracy, far higher than competing PRCs (spin torque oscillator and memristor), as shown in Figure 5b. Such good computational performance of the EDL-IGR is due to its ability to effectively exploit the complex and diverse features inherent in the ion-electron-coupled dynamics of IGR as reservoir states.[38] It was theoretically predicted that dynamical systems in the edge-of-chaos state, which is in between order and chaotic states (but in the order region), give high performance to reservoir computing.[60,61] Figure 5c shows the Lyapunov spectrum of the IGR, which was obtained by the

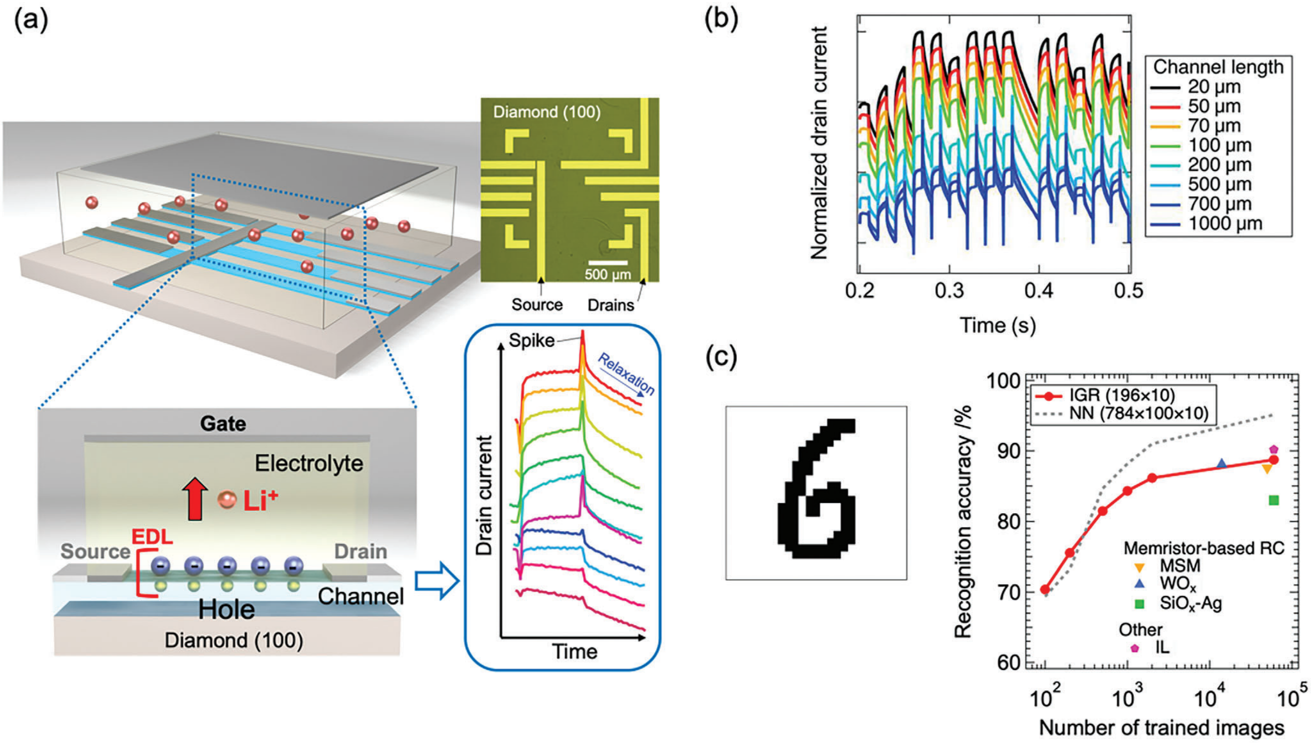

Figure 4. a) Illustrations of synaptic responses in the ion-gating reservoir (IGR) operating in an electric double-layer mechanism. b) Various drain current responses of the IGR at different channel lengths. c) Image recognition accuracy achieved by IGR as a function of the number of trained images. The dotted line shows the accuracy of a typical, full-simulation, 3-layer neural network (NN).[38] Reproduced with permission.[38] Copyright 2022, published by the American Association for the Advancement of Science.

Jacobi matrix method. The maximum Lyapunov exponent (λ_{Max}), taking a very small and negative value (-6.3×10^{-3}), supports that the IGR is on the edge of chaos state, which is suggested to be the origin of the high performance.

The performance of the EDL-IGR was further improved by the modification of operation methods.[39,40] In normal operation, the gate voltage (V_G) stream, which is converted from time series data $u(k)$, is input to the gate electrode, as shown in **Figure 6**a.[39] On the other hand, in the inverted input method, inverted input $u'(k)$ is generated by the relationship ($u'(k) = 0.5 - u(k)$). $u'(k)$ is also converted to V_G stream and input to the gate electrode. Whereas the generation of $u'(k)$ is very simple linear transformation, the method is powerful to reduce the prediction error in the second-order nonlinear equation task to as low as 50%, as shown in Figure 6b,c, supporting the notable contribution from the additional reservoir states provided by the inverted input method.

Another example of modified operation methods is deep reservoir computing.[40] Deep learning acquired its high expression power and high network flexibility through deep layering. Similar benefits of deep layering are expected to occur even in PRC

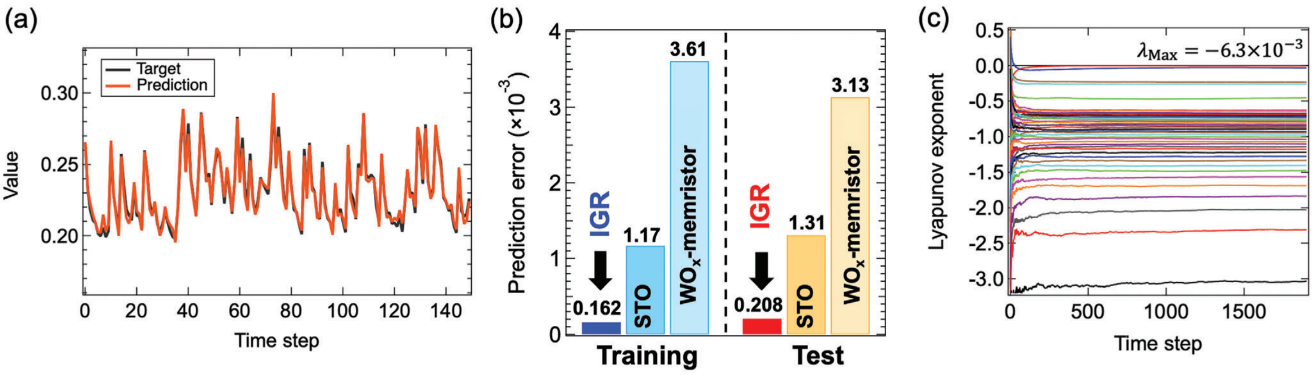

Figure 5. a) Target and prediction waveforms of 2nd order nonlinear dynamic equation at the test phase. b) Prediction error compared to other physical reservoirs. c) Lyapunov spectrum of the IGR, calculated by the Jacobi matrix method.[38] Reproduced with permission.[38] Copyright 2022, the American Association for the Advancement of Science.

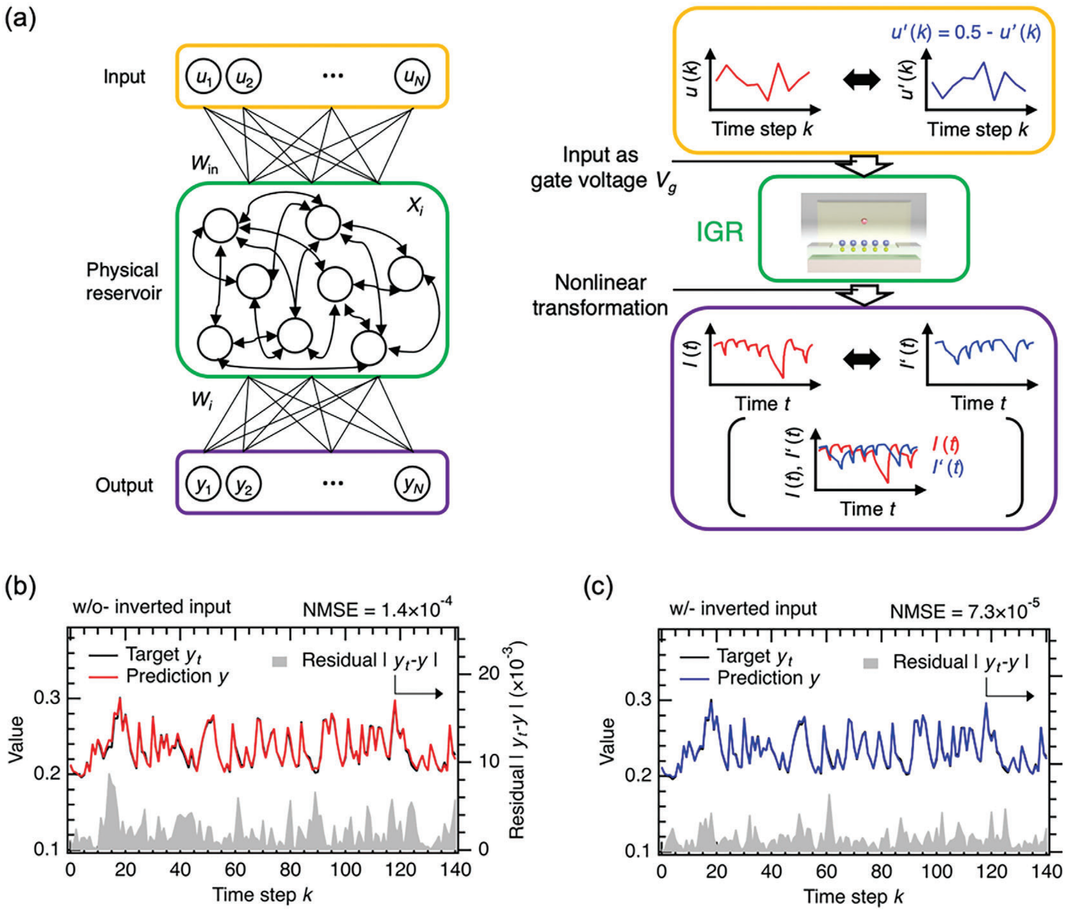

Figure 6. a) General scheme of PRC and the basic role of inverted input in PRC. The target and prediction waveforms under conditions without b) $u'(k)$ and c) with $u'(k)$ in a pulse period of 70 ms and duty rate of 70%.[39] Reproduced with permission.[39] Copyright 2024, IOP Publishing Ltd.

due to the expansion of network size, whereas an increase in computational costs is limited because a significant part of the computation is physically implemented by the dynamical behavior of physical reservoirs.[62] In this viewpoint, deep RC was applied to EDL-IGR to seek PRC performance improvement. **Figure 7a** shows a schematic diagram of deep-IGR applied to EDL-IGR.[40] One notable feature of the network is that reservoir states in reservoir layers, from the 1st to the Lth layer, are used for training in the Lth layer. In the case of EDL-IGR, only the present deep RC model gave notable performance enhancement. Figure 7b shows target and prediction waveforms for the second-order nonlinear autoregressive moving average (NARMA2), which is a typical benchmark obtained with single-layer RC and 4-layer RC. The deep RC enabled prediction error reduction by a third. Figure 7c compares the performance with the other reported PRC devices. The deep RC with EDL-IGR outperformed not only the other PRC devices but also full-simulation RC using an echo state network (ESN), which shows far better performance than known physical reservoirs.[40] The result indicates that the deep RC method is advantageous for PRC with ion-gating transistors and is further applicable to the other PRC devices toward performance enhancement.

Mobile ions other than Li^+ have been utilized for EDLT-based PRC. One is a proton. Y. Yang et al. reported a PRC device consisting of an indium-gallium-zinc-oxide (IGZO) semiconductor channel and proton conducting SiO_2 electrolyte, which was prepared by the plasma-enhanced chemical vapor method, as shown in **Figure 8a**.[41] It operates based on conductance modulation in the IGZO channel due to the EDL charging–discharging mechanism. The first EDL charging process of excitatory post-synaptic current (EPSC) response is described by the following equation:[41]

$$\Delta I = \kappa \cdot \left[1 - exp\left(-\frac{t}{\tau}\right)\right] \tag{6}$$

where κ and τ are the coefficient and time constant for the EDL charging. For the EDLT in the study, τ was calculated to be 79.26 ms, which is in the typical range of τ for EDLTs.[42] The EDLT response was applied to PRC for the spoken-digit recognition task.[41] Figure 8b shows an example of an audio waveform corresponding to the digit "nine" included in the standard NIST TI-46 database.[41] Such audio waveforms were first filtered into frequency channels. The filtered signals were preprocessed by mask matrixes for time multiplexing and were converted into gate voltage pulse trains and fed to the EDLT (reservoir). The test results are shown in Figure 8c, indicating the EDLT successfully

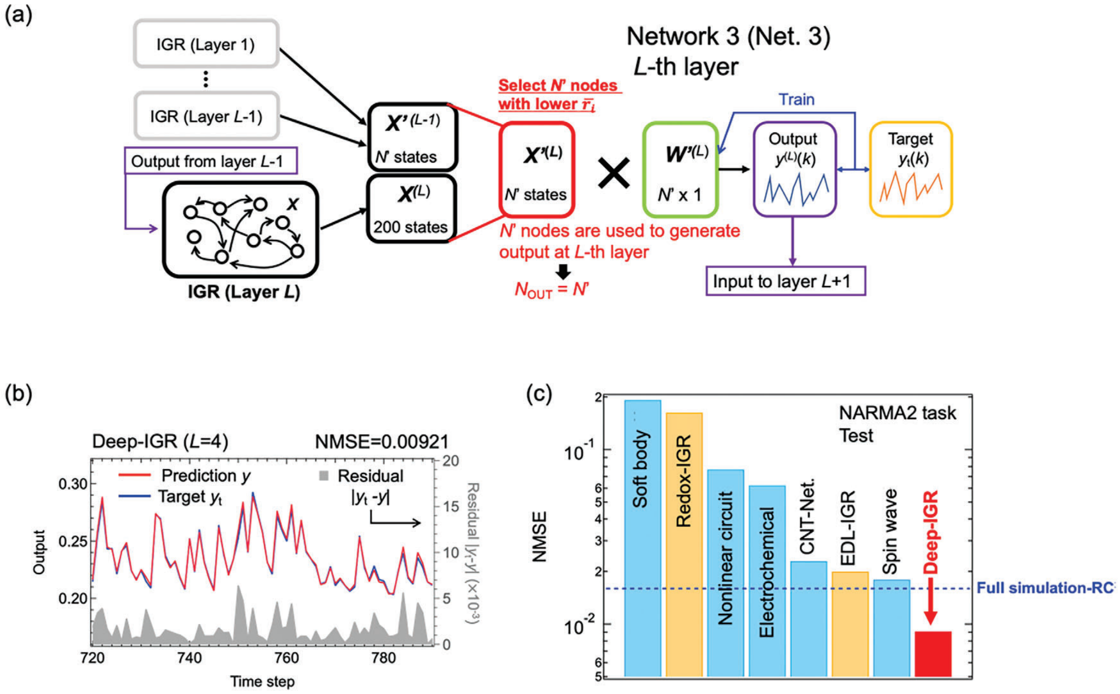

Figure 7. a) Schematic diagram of layer L of a deep-IGR (Network 3) with node selection. b) Target waveform and predicted waveform for NARMA2 task at $L = 4$. c) Performance comparison with other physical reservoirs by the second-order nonlinear autoregressive moving average (NARMA2) task.[40] Reproduced with permission.[40] Copyright 2024, Springer Nature.

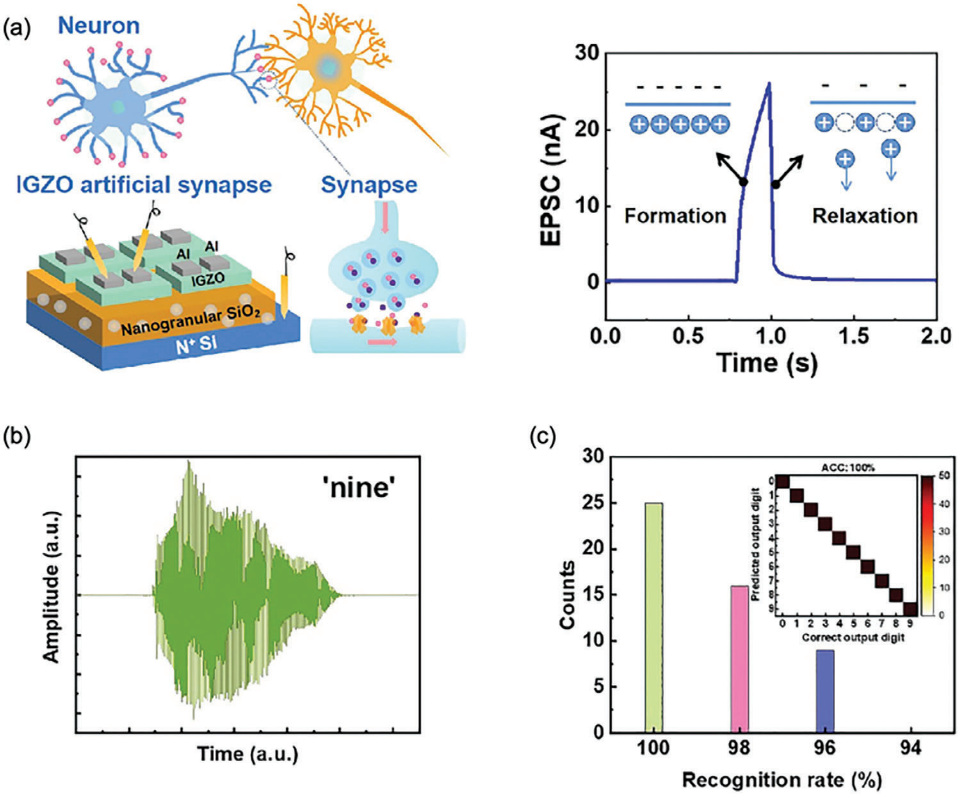

Figure 8. a) Schematic diagram of the biological neuron, synapses, and device structure. A typical EPSC triggered by a gate voltage pulse. b) Audio waveform corresponding to the digit nine pronounced by a speaker. c) Results by simulating 50 times of spoken-digit recognition tasks. Reproduced with permission.[41] Copyright 2023, AIP Publishing.

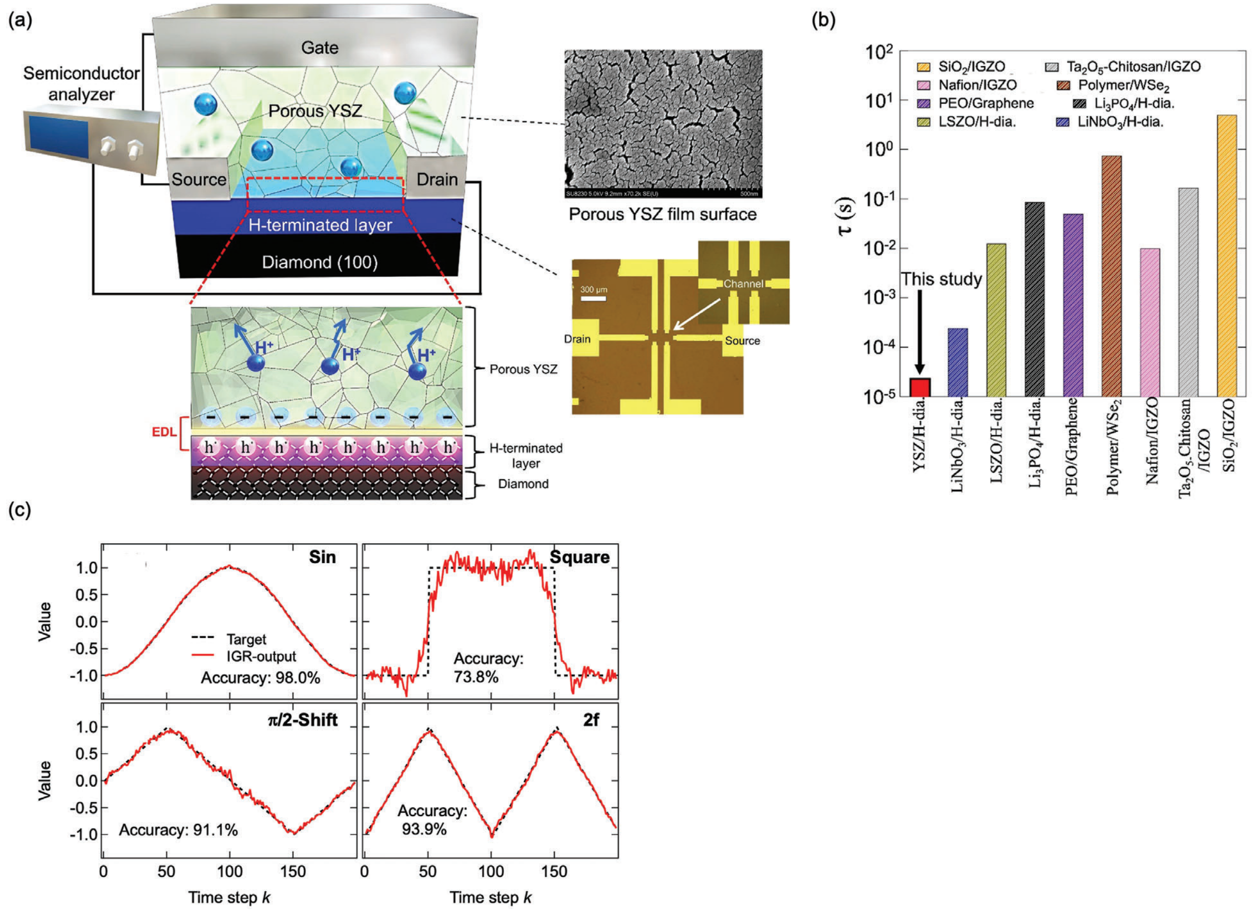

Figure 9. a) Illustration of H-diamond-based EDLT comprised of porous YSZ. b) Comparison of τ with other EDLTs. c) Generated waveform by the IGR and target waveforms for d) Sin, e) Square, f) Shift, and g) 2f.[42] Reproduced with permission.[42] Copyright 2023, Elsevier.

recognizes all of the spoken digits with low error, although cross-validation is left for reliable evaluation.[41]

Usually, inorganic solid electrolytes' ion conductivity is insufficient at RT due to low diffusion coefficient.[63] However, nanostructured oxide with meso-, nanopores, or nanograins are known to show exceptionally high proton conductivity at RT thanks to highly mobile protons provided by water molecule layers formed on the surface of pores or grains.[64–69] Takayanagi et al. fabricated an EDLT consisting of porous yttria-stabilized zirconia (YSZ) proton conductor and hydrogen-terminated diamond single crystal (100), as shown in **Figure** 9a.[42] The YSZ-EDLT showed the fastest response in reported EDLTs, with a time constant (τ) of 27 μs, due to the excellent proton conductivity of the porous YSZ thin film, as shown in Figure 9b.[42] Like Li$^+$-based EDLTs, the EDLT showed wide drain current tunability and was applied to a nonlinear waveform transformation task, a PRC benchmark. Figure 9c shows the generated waveform by the IGR and target waveforms for Sin, Square, Shift, and 2f.[42] The accuracy for the task was much better than nanowire network-type PRC except for transformation to Square wave.

In addition to Li$^+$ and H$^+$, oxide ion is a typical mobile ion for EDLTs.[70] Fang et al. utilized amorphous-TaO$_x$ thin film as an O^{2-} conducting electrolyte to fabricate EDLT for performing PRC, as shown in **Figure** 10a.[43] Electron density in the IGZO channel is reversibly tuned by EDL charging–discharging due to O^{2-} (V_O^{2+}) transport. One of the notable features of the device is the long time constant (τ) exceeding 10 s, which is advantageous for processing time series events with such a long relaxation time (e.g., earthquake, destruction of buildings, blood glucose fluctuation). It was applied to the H énon map prediction task, which is a classic discrete-time dynamic system exhibiting chaotic behavior and thus useful as a benchmark task of PRC.[43] Figure 10b shows a 2D plot of the target and output (prediction) waveforms in the testing phase, achieved with three different EDLT devices. The result shows a very low normalized root mean square error (NRMSE), supporting that the EDLT-based PRC has excellent capability. As shown in Figure 10c, NRMSE decreases as the number of EDLT devices is used as a reservoir, indicating the parallel connection of the reservoir layer is also advantageous, as well as the serial connection of the reservoir layer in deep-RC as discussed in Figure 7.

4.2. PRC Using Redox-based Ion-Gating Transistors

Redox transistors consisting of ion-electron mixed conducting channels are useful for transforming time series data through the electrical conductivity of the channel; thus, they have been

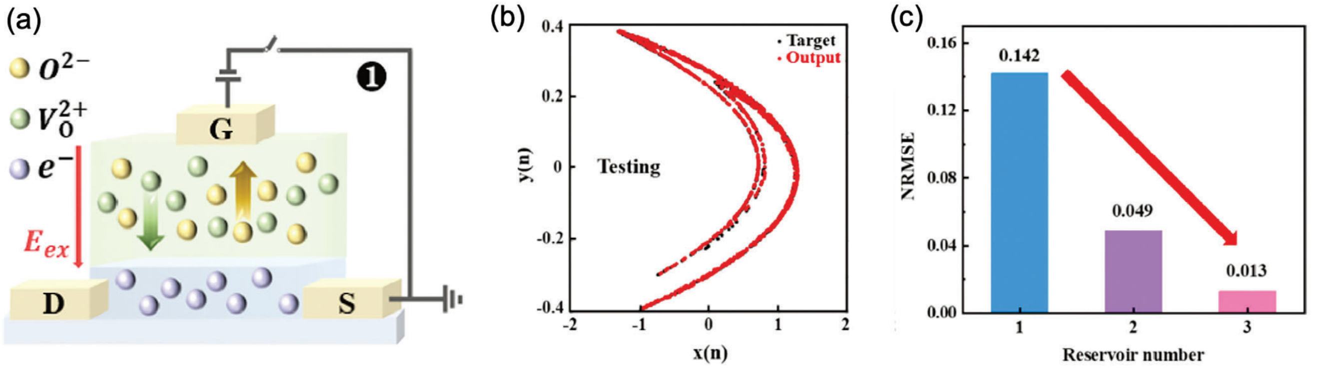

Figure 10. a) Schematic image of ionic switching mechanism for as-fabricated TaO_x-based EGT. b) The experimental output from the RC system versus the ideal target in the testing process. The result is shown as a 2D plot. c) NRMSE of the RC system integrated with different reservoir numbers.[43] Reproduced with permission.[43] Copyright 2023, Wiley.

applied to PRC. As shown in **Figure** 11a, Wada et al. fabricated a redox transistor comprising Li^+ and electron-mixed conducting Li_xWO_3 thin film, which has been a key material for electrochromic windows,[44] as the channel semiconductor material and a lithium-ion conducting glass ceramic (LICGC) substrate, of which the main crystalline component is $Li_{1+x+y}Al_xTi_{2-x}Si_yP_{3-y}O_{12}$ with NASICON (Na superionic conductor) structure accompanied with high Li^+ ion conductivity of 1×10^{-3} Scm^{-1} at RT.[71] Redox reaction of gate voltage (V_G)-driven insertion and desertion of Li^+ and electron in Li_xWO_3 thin film enables reversible electronic conductivity tuning, and the hysteretic behavior of drain current is dependent on the V_G sweep rate, as shown in Figure 11b. Due to the large Li^+ capacity (chemical capacity) of the Li_xWO_3 thin film, a significant gate current is observed in the electrical characteristic. Figure 11c shows the V_G pulse stream, drain response, and gate response during the redox-based ion-gating transistor. The drain current response shows a waveform with features different from the V_G pulse stream, supporting the transistor has a nonlinear transformation capability. An interesting point to note is that the behavior of the gate current response also differs from the one of the drain current. This enables obtaining reservoir states not only from the drain current response but also from the gate current response, as shown in Figure 11d. The double reservoir states are advantageous for improving high dimensionality based on the limited number of physical nodes of ion-gating devices. A similar approach was used for ferroelectric field effect transistors-based RC.[22]

$LiCoO_2$ is a typical cathode material for lithium-ion batteries and has also been used as a channel material for ion-gating transistors.[54,72] Shibata et al. applied a $LiCoO_2$-based redox transistor to PRC.[45] **Figure** 12a shows schematic and cross-sectional scanning electron microscope (SEM) images of the transistor consisting of a $LiCoO_2$ channel and Li^+ conducting Li_3PO_4 thin film electrolyte.[45] Physical masking was developed to improve redox-based transistors' relatively low PRC performance, as shown in Figure 12b. Masking is a method for sequentializing the input and maximizing the effectively used dimensionality of the system. It is usually done by adding a mask waveform to the original input waveform to generate the masked input waveform.[73] Although it can improve PRC performance, generating masked input requires additional processing of input waveform. However, as shown in Figure 12b, the mask waveform is directly applied to the drain electrode as drain voltage in the physical masking, omitting the additional information processing to generate the masked waveform. Figure 12c shows a comparison of reservoir states with and without physical masking. As seen from the right panels for conditions with physical masking, diverse output was attained by the method. This achieved as large as a 60 percent reduction of normalized mean square error (NMSE) for the second-order dynamic equation, supporting the notable effect of the method.

Organic gel electrolytes, as well as inorganic solid electrolytes, were used for redox-based PRC. In particular, organic electrolytes are suitable for flexible and wearable electronics. Liu et al. developed a near-sensor PRC system based on a flexible multi-gate electrolyte-gated transistor (EGT) consisting of an ion-gel electrolyte made of ionic liquid [EMI][TFSA] and polymer P(VDF-HFP) and organic semiconductor P3HT, as shown in **Figure** 13a.[46] Information detected from multiple sensors is converted to electrical voltage streams and received by the multi-gate electrodes. The voltage-driven ion transport in the electrolyte causes ion doping (redox) in the P3HT channel, leading to dynamic conductance modulation of P3HT, which is used as reservoir states for feature extraction (pre-processing) towards gait recognition (post-processing). In this work, the PRC system was used to recognize four gait patterns, including walking gait, jumping gait, festinating gait, and freezing of gait. Figure 13b shows the color confusion map showing the simulated classification results during inference, where the color confusion matrix plots the identified type as a function of the ground truth result, and the pixel darkness represents the accuracy of the corresponding results. As shown in Figure 13c, an accuracy of 93% is achieved at the maximum readout network size. Whereas a reduction in the network size deteriorates the accuracy, an accuracy of approximately 90% can still be maintained at a network size as small as 30. This work indicates the possibility of ion-gating transistor-based PRC for low-power wearable electronics, enabling on-site and real-time processing.

Ion-gating transistors have an essential function besides electrical conductivity tuning: physical properties tuning.[50–53,74–76] Electronic carrier density modulation of ion-gating transistors with magnetic materials can widely tune magnetic property

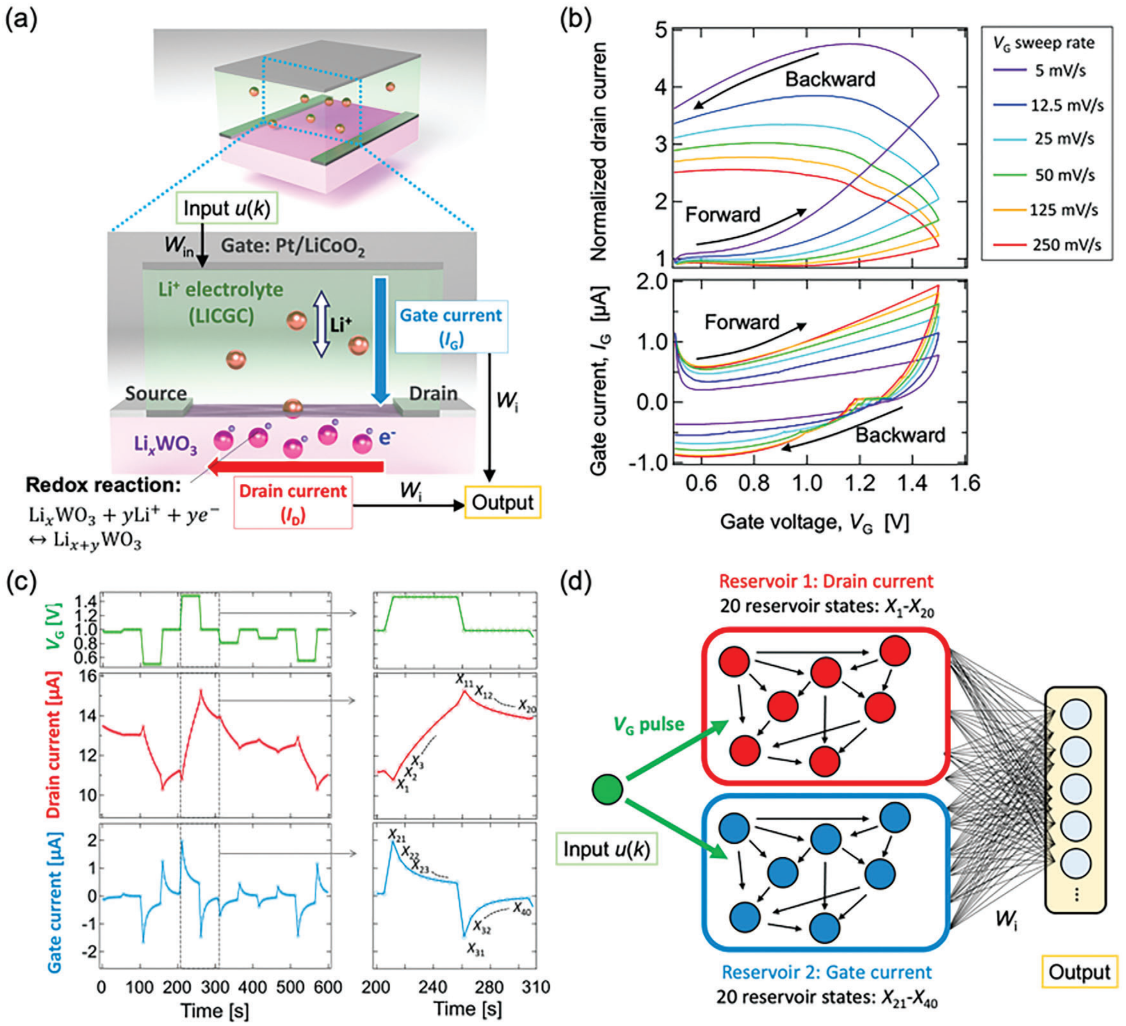

Figure 11. a) Schematic image of a Li$_x$WO$_3$-based redox-IGR. b) Normalized drain current and gate current measured during V_G sweeping. c) Gate voltage pulse stream, drain current response, and gate current response during operation of the redox-IGR. 40 reservoir states X_i (i = 1, ..., 40) are obtained as shown in the panels to the right. d) General concept of a reservoir computing system with redox-IGRs. W_i denotes the readout weight.[44] Reproduced with permission.[44] Copyright 2023, Wiley.

anisotropy,[77,78] which was applied to PRC. Namiki et al. applied a redox transistor comprising Fe$_3$O$_4$ (magnetite), which is a ferrimagnet at RT and has a large Li$^+$ capacity, and Li$^+$ conducting Li-Si-Zr-O amorphous electrolyte thin film to PRC, as shown in **Figure 14a**.[47] Fe$_3$O$_4$ has an inverse spinel structure with two Fe sites (16d octahedral site and 8a tetrahedral site), of which the oxidation state is electrochemically reduced by Li$^+$ and electron insertion accompanied by variation in magnetic anisotropy energy, leading to reversible rotation of the magnetic vector of Fe$_3$O$_4$ as shown in right panels of Figure 14a. Since electric conductivity modulation in Fe$_3$O$_4$ occurs in addition to the magnetic vector rotation, the two dynamic behaviors are utilized as computing resources to obtain reservoir states.

Magnetic vector rotation is detected by measurement of V_{XY}, corresponding to the electromotive force generated by the planar Hall effect. In contrast, electrical conductivity is detected by measuring V_{XX}, corresponding to an Ohmic drop. As shown in Figure 14b, whereas V_{XX} shows a simple waveform, V_{XY} shows a complex and characteristic waveform originating from magnetic interactions between multiple magnetic domains in Fe$_3$O$_4$ under the zero magnetic field application condition, enabling high-performance PRC. Prediction of blood glucose level fluctuation for a diabetic patient, which exhibits several ups and downs over several hours in a day, was used to evaluate the PRC performance of the devices.[47] As seen in the comparison with target and prediction waveforms of the task for 15-min-ahead prediction shown in Figure 14c, the device successfully predicted the blood glucose fluctuation behavior with root mean square error (RMSE) of 29.88 mg dl^{-1}, which is lower than the CNT-based PRC (47.0 mg dl^{-1}).[79]

Furthermore, it should be noted that the pulse period of the input voltage was 150 s, corresponding to half of the sampling time of the blood glucose level. Since it is closer to real-time processing than other cases with experimental PRCs, the device is thus helpful for real-time signal processing that matches the external signal, which has been required for PRC

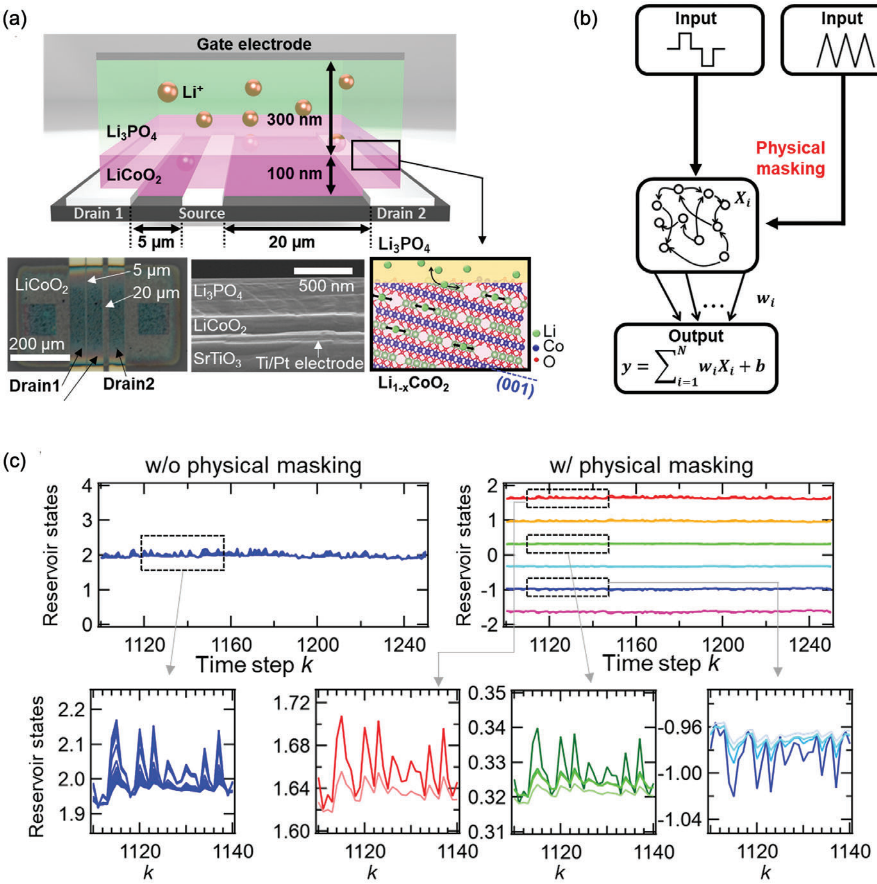

Figure 12. a) Schematic image of $LiCoO_2$-based redox-ion gating reservoir (IGR), cross-sectional SEM micrograph of a $LiCoO_2$ redox-IGR, and insertion (desertion) of Li^+ in (104) oriented $LiCoO_2$. b) RC with physical masking. (c) Reservoir state waveforms (X_1, X_2..., X_{20}) w/o and w/ physical masking.[45] Reproduced with permission.[45] Copyright 2023, Springer Nature.

but has yet to be realized. The result demonstrates the advantage of redox-based transistors in PRC for slow time series data processing.

The redox mechanism in field-effect transistors (FETs) does not necessarily require a pure electrolyte in the dielectric part. Liu et al. reported a FET consisting of a ferroelectric $Hf_{0.5}Zr_{0.5}O_2$ (HZO) film and Mott material $La_{0.67}Sr_{0.33}MnO_3$ (LSMO), as shown in **Figure 15a**.[48] In the operation cycle of the device, HZO ferroelectric thin film transfers oxide ions at the LSZO/HZO interface. For LSMO, the significant positive value of the oxygen vacancy formation energy and negative value of the oxygen affinity energy were proved based on the density function theory.[48] The inherent property of LSMO resulted in the spontaneous migration of accumulated oxygen ions in the HZO films to the channel, leading to characteristic behavior, including volatile and nonvolatile oxide ion dynamics at the LSZO/HZO interface shown in Figure 15b. The electrical characteristic of the device was applied to PRC-based human voice recognition. The variations in voice amplitude signal, for five English words spoken by four people, as a function of time converted to magnitude signal versus frequency through the Fast Fourier Transform (FFT) process. They were further converted to binary data and used to input data for PRC, as shown in Figure 15c. The PRC system showed good recognition properties. The result indicates that the exploration of ionic phenomena-based PRC can be further extended to non-electrolyte systems.

4.3. Comparison Based on Materials, Machine Learning Tasks and Operating Mechanisms

The PRCs introduced in the previous sections are compared based on their materials, machine-learning tasks, and operating mechanisms. **Table 1** summarizes materials and machine learning tasks used for PRC devices in the form of ion-gating transistors. Regarding electrolyte materials, they are broadly divided into inorganic materials with Li^+, H^+, and O^{2-} conduction and ion-gels (organic materials). When inorganic materials are used, devices are fabricated using various thin film growth methods (e.g., pulse laser ablation, sputtering), so it is easy to apply microfabrication, and relatively small devices (μm to nm size) were fabricated,[38,41,42,48] while when organic materials (ion-gel) are used, it seems that relatively large-sized devices (mm size) are fabricated.[46] This is a general trend that applies not only to PRC devices but also to general electronic devices to some extent, and it will be related to the integration of PRC devices in the future. As for the machine learning tasks, handwritten-digit recognition, second-order nonlinear dynamic equation, and NARMA tasks

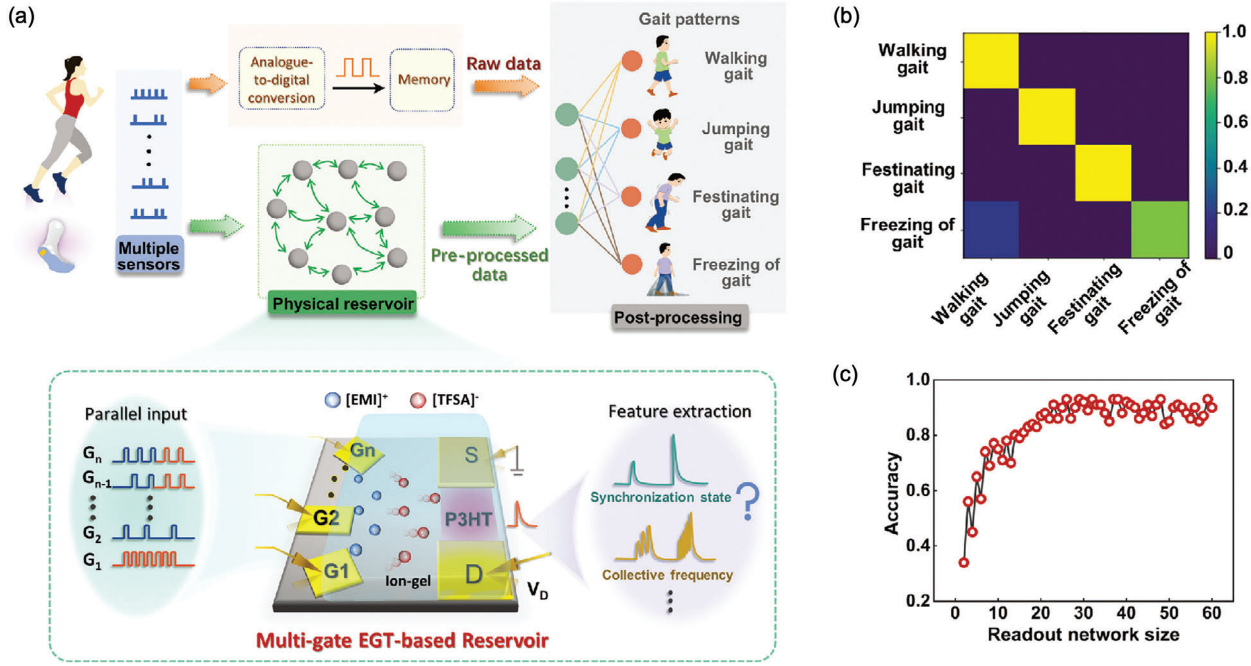

Figure 13. a) Comparison between the digital computing and near-sensor RC schemes for gait recognition. In the near-sensor RC case, the data are pre-processed by the physical reservoir for key feature extraction, which largely reduces the data amount for post-processing, significantly improving the efficiency. Illustration of a flexible multi-gate electrolyte-gated transistor (EGT) as a reservoir for parallel signal processing, enabling the extraction of temporal features such as the synchronization state and collective frequency. b) False color confusion map showing the simulated identification results. The occurrence probability for each gait pattern is represented by the colors in the color scale. c) Recognition accuracy as a function of readout network size.[46] Reproduced with permission.[46] Copyright 2023, Wiley.

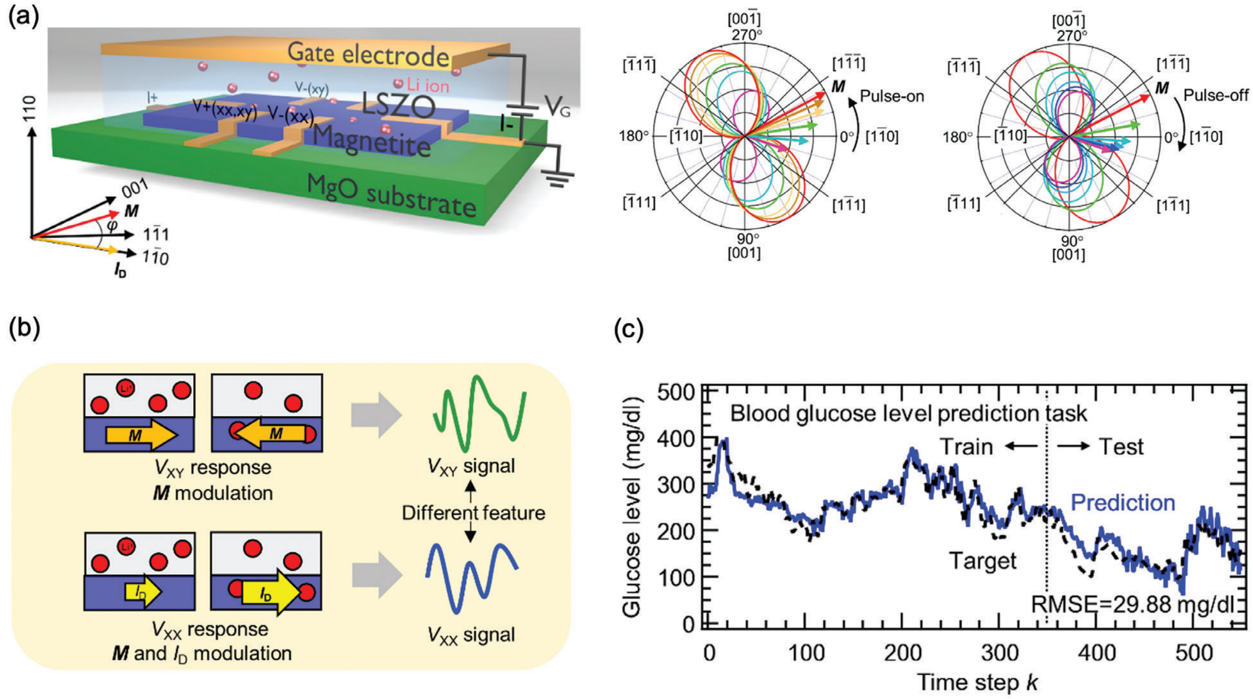

Figure 14. a) Schematic illustrations of (left) the magnetization vector rotation reservoir device. φ is defined as the relative angle between the electric current I_D and magnetization M, and (right) the magnetic anisotropy and magnetization vector. b) Schematic illustration of V_{XY} and V_{XX} responses to a pulsed voltage. c) Target and prediction waveforms of blood glucose level prediction with a magnetization vector rotation reservoir. Black and blue solid lines denote target and prediction waveforms, respectively.[47] Reproduced with permission.[47] Copyright 2024, American Chemical Society.

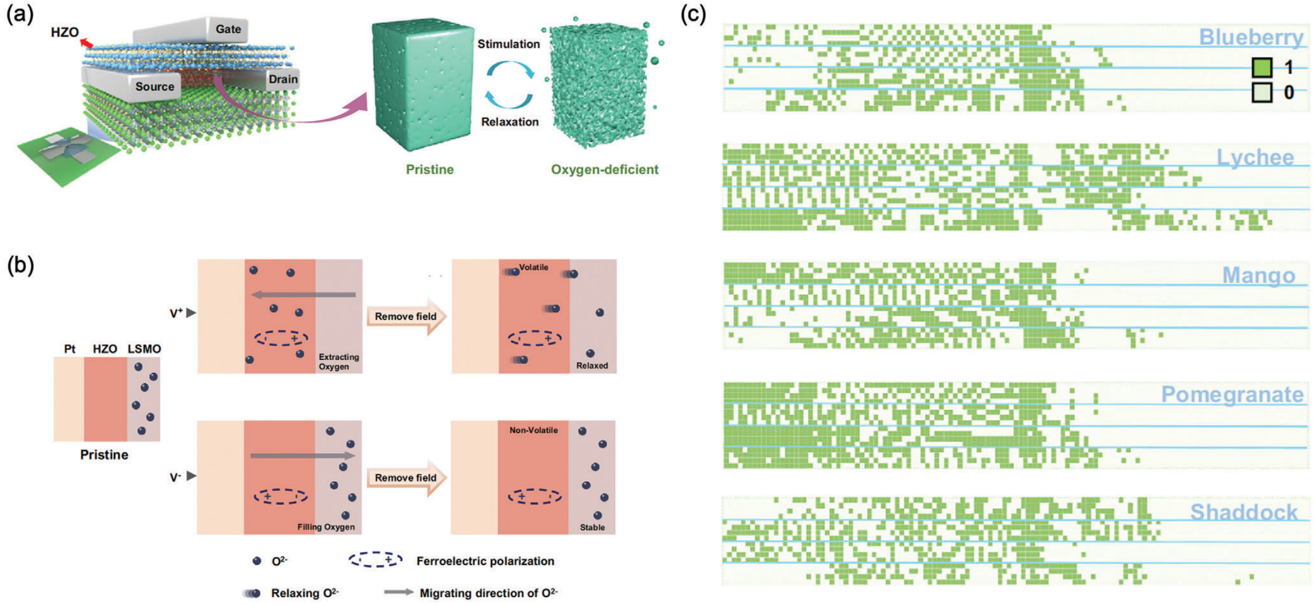

Figure 15. a) Device structure of ferroelectric $Hf_{0.5}Zr_{0.5}O_2$-based FET and the structural transition between the pristine and oxygen-deficient phases. b) Schematic illustration of volatile and nonvolatile regulation during the gating process in the proposed device. c) All input data consists of five English words spoken by four people in human voice recognition.[48] Reproduced with permission.[48] Copyright 2023,Springer Nature.

have been relatively common. However, it is difficult to accurately compare the computational performance among all the devices at present, as there is no common benchmark task for all, but the comparison will become possible as research progresses and NARMA or the other typical tasks become more common.

When comparing the operating mechanisms, the fastest systems using EDLs have time constants of 27 µs, which is relatively fast, whereas, in redox systems, time constants of several hundred seconds have been reported, so there is a difference in response speed, with EDL systems being relatively fast and redox systems being slow.[42,48] This is because, as discussed in the previous sections, the EDL system's control of electron carriers corresponds to the behavior of charge carriers (ion and electron/hole) in the very vicinity of the electrolyte/semiconductor

Table 1. Summary of materials and machine learning tasks used for PRC devices in the form of ion-gating transistors.

Materials					Machine learning tasks
Electrolyte				Semiconductor	
Li^+ conductor	H^+ conductor	O^{2-} conductor	Ion-gel		
LSZO[39,40] LICGC[44] Li_3PO_4[45]	Porous YSZ[42] Nanogranular SiO_2[41]	Amorphous-TaO_x[43] HZO[48]	[EMI][TFSA] – P(VDF-HFP)[46]	LSMO[48] Fe_3O_4 [47] Diamond[38–40,42] IGZO[41,43] WO_x[44] $LiCoO_2$[45] P3HT[46]	Nonlinear waveform transformation[42] Handwritten- digit recognition[38,41,43] Digital letter classification[48] Human voice recognition[48] Speech digital recognition[41] Gait identification[46] Second-order nonlinear dynamic equation[38,39,44,45] NARMA[38,40,44,45] Hénon map prediction[43,48] Blood glucose level prediction[47]

Table 2. Comparison of operation speed for reported PRC devices.

	Ion-gating transistors		Electrochemical reaction	Memristors	Optoelectronic circuits	Spintronics
	EDL type	Redox type				
Operation speed (e.g., time constant)	27 µs (diamond-porous YSZ)[42] ≈1 ms (diamond-LSZO)[38] 79 ms (IGZO-nanogranular SiO_2)[41] 22 ms (IGZO-amorphous-TaO_x)[43]	26.9 s (LSMO-HZO)[48] 68.0 s (LSZO-Fe_3O_4)[47]	Several ms (Polyoxometalate solution)[19]	50 ms (WO_x)[16]	8.504 µs (for the round trip time)[21]	Several tens ns (spin wave $Y_3Fe_5O_{12}$)[27] Several tens ns (spin torque oscillator)[23]

interface, whereas the redox system relies on relatively slow carrier transport throughout the mixed conductor channel. Comparison of operation speed is compared with other PRC devices including optoelectronic circuits, memristors, and spintronics devices, in **Table** 2. While ion-gating transistors show relatively low operation speed with respect to optoelectronic circuits or spintronics devices, it has a wide range from µs to several hundred seconds. The difference in operation speed (or time constant) is not a matter of which is better, as it can be selected according to the time constant of the signal to which the PRC is applied.

5. Conclusion

Recent advances in PRC utilizing electrical responses of ion-gating transistors have been outlined. Ion-gating transistors, which can use two types of electrochemical processes—the EDL and redox—to control electrical conductivity, gives a variety of electrical characteristics (including transient behavior) depending on the choice of electrolyte (Li^+, H^+, O^{2-}, ion-gels) and semiconductor materials (IGZO, WO_x, $LiCoO_2$, diamond, P3HT, etc.), device structure (simple transistor, multi-terminal), etc. Utilizing the ion-gating transistors for PRC, it is possible to obtain the nonlinearity, short-term memory, and high dimensionality required for achieving high information capability. While the PRC performance of ion-gating transistors has been evaluated on the basis of some typical machine learning tasks including handwritten-digit recognition, NARMA, and second-order nonlinear dynamic equation tasks, which are relatively simple and equation-based dynamical systems, the PRC devices will be further applied to more practical tasks under the real environment as the performance improves. Electrochemical systems are a treasure trove of diversity and complexity, which is highly advantageous for high-performance information processing. Ion-gating transistors can realize such features of electrochemical systems in the nano space of a thin-film device,[80–84] making them helpful in building highly integrated information processing systems. Furthermore, due to the high degree of structural freedom, they have a high affinity with excellent functional materials, such as low-dimensional materials and high-dimensional nanostructured materials,[85–91] which have been studied in recent years and can be combined to achieve dramatic performance improvements. Ion-gating transistors are a promising frontier for developing next-generation neuromorphic devices to solve the severe energy problems that current artificial intelligence technology faces.

Acknowledgements

This work was partly supported by the JST PRESTO Grant number, JPMJPR23H4, and the Japan Society for the Promotion of Science (JSPS) KAKENHI Grant number, 24KJ0229.

Conflict of Interest

The authors declare no conflict of interest.

Keywords

ion-gating reservoirs, ion-gating transistors, reservoir computing, solid state ionics

Received: August 10, 2024
Revised: October 29, 2024
Published online: November 20, 2024

---

[1] Y. LeCun, Y. Bengio, G. Hinton, *Nature* **2015**, *521*, 436.
[2] M. Jovanović, M. Campbell, *Computer* **2022**, *55*, 107.
[3] D. Kramer, *Phys. Today.* **2024**, *77*, 28.
[4] M. Davis, N. Srinivasa, T.-H. Lin, G. Chinya, Y. Cao, S. H. Choday, *IEEE Micro.* **2018**, *38*, 82.
[5] F. Aguirre, A. Sebastian, M. L. Gallo, W. Song, T. Wang, J. J. Yang, W. Lu, M.-F. Chang, D. Ielmini, Y. Yang, A. Mehonic, A. Kenyon, M. A. Villena, J. B. Roldan, Y. Wu, H.-H. Hsu, N. Raghavan, J. Sune, E. Miranda, A. Eltawil, G. Setti, K. Smagulova, K. N. Salama, O. Krestinskaya, X. Yan, K.-W. Ang, S. Jain, S. Li, O. Alharbi, S. Pazos, et al., *Nat. Commun.* **2024**, *15*, 1974.
[6] W. Wan, R. Kubendran, C. Schaefer, S. B. Eryilmaz, W. Zhang, D. Wu, S. Deiss, P. Raina, He Qian, B. Gao, S. Joshi, H. Wu, H.-S. P Wong, G. Cauwenberghs, *Nature* **2022**, *608*, 504.
[7] Q. Wan, F. Zeng, J. Yin, Y. Sun, Y. Hu, J. Liu, Y. Wang, G. Li, D. Guo, F. Pan, *Nanoscale* **2019**, *11*, 5684.
[8] J. Yu, F. Zeng, Q. Wan, Y. Sun, L. Qiao, T. Chen, H. Wu, Z. Zhao, J. Cao, F. Pan, *Nano Res.* **2022**, *15*, 8410.
[9] H. Jaeger, H. Haas, *Science* **2004**, *304*, 78.
[10] H. Jaeger, *The "echo state" approach to analyzing and training recurrent neural networks with an erratum note*, German National Research

Center for Information Technology GMD Technical Report, Bonn, Germany **2001**, *148*, 13.
[11] W. Maass, T. Natschläger, H. Markram, *Neural Comput.* **2002**, *14*, 2531.
[12] G. Tanaka, T. Yamane, J. B. Héroux, R. Nakane, N. Kanazawa, S. Takeda, H. Numata, D. Nakano, A. Hirose, *Neural Netw.* **2019**, *115*, 100.
[13] K. Nakajima, H. Hauser, T. Li, R. Pfeifer, *Sci. Rep.* **2015**, *5*, 10487.
[14] H. O. Sillin, R. Aguilera, H. H. Shieh, A. V. Avizienis, M. Aono, A. Z. Stieg, J. K. Gimzewski, *Nanotechnology* **2013**, *24*, 384004.
[15] S. Lilak, W. Woods, K. Scharnhorst, C. Dunham, C. Teuscher, A. Z. Stieg, J. K. Gimzewski, *Front. Nanotechnol.* **2021**, *3*, 675792.
[16] C. Du, F. Cai, M. A. Zidan, W. Ma, S. H. Lee, W. D. Lu, *Nat. Commun.* **2017**, *8*, 2204.
[17] M. Akai-Kasaya, Y. Takeshima, S. Kan, K. Nakajima, T. Oya, T. Asai, *Neuromorph. Comput. Eng.* **2022**, *2*, 014003.
[18] Y. Usami, B. van de Ven, D. G. Mathew, T. Chen, T. Kotooka, Y. Kawashima, Y. Tanaka, Y. Otsuka, H. Ohoyama, H. Tamukoh, H. Tanaka, W. G. van der Wiel, T. Matsumoto, *Adv. Mater.* **2021**, *33*, 2102688.
[19] S. Kan, K. Nakajima, T. Asai, M. Akai-Kasaya, *Adv. Sci.* **2022**, *9*, 2104076.
[20] S. G. Koh, H. Shima, Y. Naitoh, H. Akinaga, K. Kinoshita, *Sci. Rep.* **2022**, *12*, 6958.
[21] Y. Paquot, F. Duport, A. Smerieri, J. Dambre, B. Schrauwen, M. Haelterman, S. Massar, *Optoelectron. Reservo. Comput. Sci. Rep.* **2012**, *2*, 287.
[22] K. Toprasertpong, E. Nako, Z. Wang, R. Nakane, M. Takenaka, S. Takagi, *Commun. Eng.* **2022**, *1*, 21.
[23] S. Tsunegi, T. Taniguchi, K. Nakajima, S. Miwa, K. Yakushiji, A. Fukushima, S. Yuasa, H. Kubota, *Appl. Phys. Lett.* **2019**, *114*, 164101.
[24] J. Torrejon, M. Riou, F. A. Araujo, S. Tsunegi, G. Khalsa, D. Querlioz, P. Bortolotti, V. Cros, K. Yakushiji, A. Fukushima, H. Kubota, S. Yuasa, M. D. Stiles, J. Grollier, *Nature* **2017**, *547*, 428.
[25] R. Nakane, G. Tanaka, A. Hirose, *IEEE Access* **2018**, *6*, 4462.
[26] R. Nakane, A. Hirose, G. Tanka, *Phys. Rev. Appl.* **2023**, *19*, 034047.
[27] W. Namiki, D. Nishioka, Y. Yamaguchi, T. Tsuchiya, T. Higuchi, K. Terabe, *Adv. Intell. Syst.* **2023**, *5*, 2300228.
[28] W. Namiki, Y. Yamaguchi, D. Nishioka, T. Tsuchiya, K. Terabe, *Mater. Today Phys.* **2024**, *45*, 101465.
[29] W. Namiki, D. Nishioka, T. Tsuchiya, K. Terabe, *Neuromorphic Comput. Engin.* **2024**, *4*, 024015.
[30] S. Kan, K. Nakajima, Y. Takeshima, T. Asai, Y. Kuwahara, M. Akai-Kasaya, *Phys. Rev. Appl.* **2021**, *15*, 024030.
[31] J. Moon, W. Ma, J. H. Shin, F. Cai, C. Du, S. H. Lee, W. D. Lu, *Nat. Electron.* **2019**, *2*, 480.
[32] R. Midya, Z. Wang, S. Asapu, X. Zhang, M. Rao, W. Song, Y. Zhuo, N. Upadhyay, Q. Xia, J. J. Yang, *Adv. Intell. Syst.* **2019**, *1*, 1900084.
[33] X. Zhu, Q. Wang, W. D. Lu, *Nat. Commun.* **2020**, *11*, 2439.
[34] L. Sun, Z. Wang, J. Jiang, Y. Kim, B. Joo, S. Zheng, S. Lee, W. J. Yu, B. S. Kong, H. Yang, *Sci. Adv.* **2021**, *7*, eabg1455.
[35] Y. Zhong, J. Tang, X. Li, B. Gao, H. Qian, H. Wu, *Nat. Commun.* **2021**, *12*, 408.
[36] J. Hochstetter, R. Zhu, A. Loeffler, A. D. Alvarez, T. Nakayama, Z. Kuncic, *Nat. Commun.* **2021**, *12*, 4008.
[37] G. Milano, G. Pedretti, K. Montano, S. Ricci, S. Hashemkhani, L. Boarino, D. Ielmini, C. Ricciardi, *Nat. Mater.* **2022**, *21*, 195.
[38] D. Nishioka, T. Tsuchiya, W. Namiki, M. Takayanagi, M. Imura, Y. Koide, T. Higuchi, K. Terabe, *Sci. Adv.* **2022**, *8*, eade1156.
[39] Y. Yamaguchi, D. Nishioka, W. Namiki, T. Tsuchiya, M. Imura, Y. Koide, T. Higuchi, K. Terabe, *Appl. Phys. Express* **2024**, *17*, 024501.
[40] D. Nishioka, T. Tsuchiya, M. Imura, Y. Koide, T. Higuchi, K. Terabe, *Communication. Engin.* **2024**, *3*, 81.
[41] Y. Yang, H. Cui, S. Ke, M. Pei, K. Shi, C. Wan, Q. Wan, *Appl. Phys. Lett.* **2023**, *122*, 043508.
[42] M. Takayanagi, D. Nishioka, T. Tsuchiya, M. Imura, Y. Koide, T. Higuchi, K. Terabe, *Mater. Today Adv.* **2023**, *18*, 100393.
[43] R. Fang, S. Wang, W. Zhang, K. Ren, W. Sun, F. Wang, J. Lai, P. Zhang, X. Xu, Q. Luo, L. Li, Z. Wang, D. Shang, *Adv. Electron. Mater.* **2024**, *10*, 2300652.
[44] T. Wada, D. Nishioka, W. Namiki, T. Tsuchiya, T. Higuchi, K. Terabe, *Adv. Intellig. Syst.* **2023**, *5*, 2300123.
[45] K. Shibata, D. Nishioka, W. Namiki, T. Tsuchiya, T. Higuchi, K. Terabe, *Sci. Rep.* **2023**, *13*, 21060.
[46] X. Liu, C. Sun, Z. Guo, X. Xia, Q. Jiang, X. Ye, J. Shang, Y. Zhang, X. Zhu, R. W. Li, *Adv. Sci.* **2023**, *10*, 2300471.
[47] W. Namiki, D. Nishioka, T. Tsuchiya, T. Higuchi, K. Terabe, *Nano Lett.* **2024**, *24*, 4383.
[48] Z. Liu, Q. Zhang, D. Xie, M. Zhang, X. Li, H. Xhong, G. Li, M. He, D. Shang, C. Wang, L. Gu, G. Yang, K. Jin, C. Ge, *Nat. Commun.* **2023**, *14*, 7176.
[49] D A. Allwood, M O. A. Ellis, D. Griffin, T J. Hayward, L. Manneschi, M F. Kh. Musameh, S. O'Keefe, S. Stepney, C. Swindells, M A. Trefzer, E. Vasilaki, G. Venkat, I. Vidamour, C. Wringe, *Appl. Phys. Lett.* **2023**, *12*, 040501.
[50] K. Terabe, T. Tsuchiya, R. Yang, M. Aono, *Nanoscale* **2016**, *8*, 138739.
[51] T. Tsuchiya, K. Terabe, R. Yang, M. Aono, *Jpn. J. Appl. Phys.* **2016**, *55*, 1102A4.
[52] K. Terabe, T. Tsuchiya, T. Tsuruoka, *Complementing Electron. Compon. Adv. Electron. Mater.* **2016**, *8*, 21006452022
[53] K. Terabe, T. Tsuchiya, T. Tsuruoka, *Jpn. J. Appl. Phys.* **2022**, *61*, SM0803.
[54] E J. Fuller, F El Gabaly, F. Léonard, S. Agarwal, S J. Plimpton, R B. Jacobs-Gedrim, C D. James, M J. Marinella, A. A Talin, *Adv. Mater.* **2017**, *29*, 1604310.
[55] T. Tsuchiya, M. Imura, Y. Koide, K. Terabe, *Sci. Rep.* **2017**, *7*.
[56] T. Tsuchiya, S. Moriyama, K. Terabe, M. Aono, *Appl. Phys. Lett.* **2015**, *107*, 10534.
[57] T. Tsuchiya, K. Terabe, M. Aono, *Appl. Phys. Lett* **2014**, *18*, 183101.
[58] T. Tsuchiya, Y. Itoh, Y. Yamaoka, S. Ueda, Y. Kaneko, T. Hirasawa, M. Suzuki, K. Terabe, *J. Phys. Chem. C* **2019**, *123*, 104873.
[59] T. Tsuchiya, M. Takayanagi, K. Mitsuishi, M. Imura, S. Ueda, Y. Koide, T. Higuchi, K. Terabe, *Commun. Chem.* **2021**, *4*, 117.
[60] M. Inubushi, K. Yoshimura, *Sci. Rep.* **2017**, *7*, 10199.
[61] J. Hochstetter, R. Zhu, A. Loeffler, A. Diaz-Alvarez, T. Nakayama, Z. Kuncic, *Nat. Commun.* **2021**, *12*, 4008.
[62] M. Nakajima, K. Inoue, K. Tanaka, Y. Kuniyoshi, T. Hashimoto, K. Nakajima, *Nat. Commun.* **2022**, *13*, 7847.
[63] O. Yamamoto, *Sci. Technol. Adv. Mater.* **2017**, *18*, 504.
[64] B. Scherrer, M. V. F. Schlupp, D. Stender, J. Martynczuk, J. G. Grolig, H. Ma, P. Kocher, T. Lippert, M. Prestat, L. J. Gauckler, *Adv. Funct. Mater.* **2013**, *23*, 1957.
[65] D. Etoh, T. Tsuchiya, M. Takayanagi, T. Higuchi, K. Terabe, *Jpn. J. Appl. Phys.* **2019**, *58*, SDDG01.
[66] M. Takayanagi, T. Tsuchiya, D. Nishioka, T. Higuchi, K. Terabe, *J. Mater. Chem. C.* **2023**, *11*, 133113.
[67] M. Takayanagi, T. Tsuchiya, K. Kawamura, M. Minohara, K. Horiba, H. Kumigashira, T. Higuchi, *Solid State Ionics* **2017**, *311*, 46.
[68] T. Tsuchiya, K. Terabe, M. Aono, *Adv. Mater.* **2014**, *26*, 1087.
[69] T. Tsuchiya, M. Ochi, T. Higuchi, K. Terabe, M. Aono, *ACS Appl. Mater. Interfaces* **2015**, *7*, 122540.
[70] T. Tsuchiya, K. Terabe, M. Aono, *Appl. Phys. Lett.* **2013**, *103*, 073110.
[71] H. Aono, E. Sugimoto, Y. Sadaoka, N. Imanaka, G. Adachi, *Chem. Lett.* **1991**, *20*, 1567.
[72] K. Kawashima, T. Ohnishi, K. Takada, *ACS Appl. Energy Mater.* **2020**, *3*, 11803.

[73] L. Appeltant, G. Van der Sande, J. Danckaert, I. Fischer, *Sci. Rep.* **2014**, *4*, 3629.
[74] K. Ueno, S. Nakamura, H. Shimotani, A. Ohtomo, N. Kimura, T. Nojima, H. Aoki, Y. Iwasa, M. Kawasaki, *Nat. Mater.* **2008**, *7*, 855.
[75] J. T. Ye, Y. J. Zhang, R. Akashi, M. S. Bahramy, R. Arita, Y. Iwasa, *Science* **2008**, *338*, 11932012
[76] M. Nakano, K. Shibuya, D. Okuyama, T. Hatano, S. Ono, M. Kawasaki, Y. Iwasa, Y. Tokura, *Nature* **2012**, *487*, 459.
[77] T. Tsuchiya, K. Terabe, M. Ochi, T. Higuchi, M. Osada, Y. Yamashita, S. Ueda, M. Aono, *ACS Nano* **2016**, *10*, 1655.
[78] W. Namiki, T. Tsuchiya, M. Takayanagi, T. Higuchi, K. Terabe, *ACS Nano* **2020**, *14*, 160652.
[79] T. Shingu, H. Uchiyama, T. Watanabe, Y Ohno, *Carbon* **2023**, *214*, 118344.
[80] T. Tsuchiya, S. Miyoshi, Y. Yamashita, H. Yoshikawa, K. Terabe, K. Kobayashi, S. Yamaguchi, *Sci. Technol. Adv. Mater.* **2013**, *14*, 045001.
[81] T. Tsuchiya, S. Miyoshi, Y. Yamashita, H. Yoshikawa, K. Terabe, K. Kobayashi, S. Yamaguchi, *Solid State Ionics* **2013**, *253*, 110.
[82] M. Takayanagi, T. Tsuchiya, S. Ueda, T. Higuchi, K. Terabe, *Appl. Surf. Sci.* **2021**, *568*, 150898.
[83] M. Takayanagi, T. Tsuchiya, D. Nishioka, M. Imura, Y. Koide, T. Higuchi, K. Terabe, *Mater. Today Phys.* **2023**, *31*, 101006.
[84] D. Nishioka, T. Tsuchiya, T. Higuchi, K. Terabe, *Neuromorphic Comput. Engin.* **2023**, *3*, 034008
[85] H. Zhang, T. Tsuchiya, C. Liang, K. Terabe, *Nano Lett.* **2015**, *15*, 5161.
[86] D. Nishioka, Y. Shingaya, T. Tsuchiya, T. Higuchi, K. Terabe, *Sci. Adv.* **2024**, *10*, eadk6438.
[87] T. Tsuchiya, T. Nakayama, K. Ariga, *Appl. Phys. Express.* **2022**, *15*, 100101.
[88] K. Ariga, *Materials* **2024**, *17*, 271.
[89] K. Ariga, *Micromachines.* **2024**, *15*, 282
[90] R. Nur, T. Tsuchiya, K. Toprasertpong, K. Terabe, S. Takagi, M. Takenaka, *Nanoscale* **2022**, *14*, 2013.
[91] T. Tsuchiya, T. Tsuruoka, K. Terabe, M. Aono, *ACS Nano* **2015**, *9*, 2102.

Takashi Tsuchiya is the Group Leader of the Neuromorphic Devices Group at the Research Center for Materials Nanoarchitectonics (MANA), National Institute for Materials Science (NIMS) in Japan. His research interest and activities are concentrated on spatiotemporal dynamics of ions, electrons, and spin in nanoscale regions in materials and their applications to neuromorphic computing. He received a B.S. degree, an M.S. degree, and a Ph.D. degree from the University of Tokyo, all in materials science and engineering. After studying as a Postdoctoral Researcher at the University of Tokyo, NIMS, and the Tokyo University of Science, he obtained a permanent position at NIMS.

Daiki Nishioka received his Ph.D. from Tokyo University of Science in 2024, specializing in brain-inspired computing with a focus on ionic device applications. He joined the International Center for Young Scientists (ICYS) at the National Institute for Materials Science (NIMS) as an ICYS Research Fellow in 2024. Daiki Nishioka's work centers on advancing neuromorphic computing through nanoionic devices. His research tackles the design of physical reservoir computing systems and artificial synapses, leveraging nanoionic phenomena to emulate biological processes for efficient, high-performance computing. Emphasizing innovative architectures, he aims to bridge nanoionics and neuromorphic engineering, advancing applications in AI and beyond.

Wataru Namiki received his Ph.D. degree from Tokyo University of Science in 2021. He joined the National Institute for Materials Science (NIMS) as a Postdoc researcher in 2021 and is currently working as a Researcher in the Ionic Devices Group of the World Premier International (WPI) Research Center for Materials Nanoarchitectonics (MANA), the NIMS. His current research focuses on high-efficient neuromorphic computing devices including physical reservoir computing based on ionic and spintronic phenomena.

Kazuya Terabe is a group leader at the Research Center for Materials Nanoarchitectonics (MANA), National Institute for Materials Science (NIMS), Japan. He received his Ph.D. from Nagoya Institute of Technology in 1992. Before joining NIMS in 2003, he was a special postdoctoral researcher at RIKEN and an assistant professor at Nagoya University. His current research focuses on the creation of nanoionic devices that enable multiple functionalities, the development of nanoionics technology-enhanced electronic devices, and the application of such devices and circuits to information communication and artificial intelligence systems.